The current issue and full text archive of this journal is available at
www.emeraldinsight.com/0961-5539.htm

Numerical simulation of channel segregates during alloy solidification using TVD schemes

Mohamed Rady
TREFLE, Université de Bordeaux, Bordeaux, France, and FAST, Université Paris VI et Paris XI, Paris, France
Eric Arquis
TREFLE, Université de Bordeaux, Bordeaux, France
Dominique Gobin
FAST, Université Paris VI et Paris XI, Paris, France, and
Benoît Goyeau
EM2C, Ecole Centrale Paris, Paris, France

Received 25 May 2009
Revised 3 September 2009
Accepted 20 October 2009

Abstract

Purpose – This paper aims to tackle the problem of thermo-solutal convection and macrosegregation during ingot solidification of metal alloys. Complex flow structures associated with the development of channels segregate and sharp gradients in the solutal field call for the implementation of accurate methods for numerical modeling of alloy solidification. In particular, the solute transport equation is convection dominated and requires special non-oscillarity type high-order schemes to handle the regions of channels segregates.

Design/methodology/approach – In the present study, a time-splitting approach has been adopted to separately handle solute advection and diffusion. This splitting technique allows the application of accurate total variation dimensioning (TVD) schemes for solution of solute advection. Applications of second-order Lax-Wendroff TVD SUPERBEE and fifth-order weighted essentially non-oscillatory (WENO) schemes are described in the present article. Classical numerical solution of solute transport using hybrid and central-difference schemes are also employed for the purpose of comparisons. Numerical simulations for solidification of Pb-18%Sn in a two-dimensional rectangular cavity have been carried out using different numerical schemes.

Findings – Numerical results show the difficulty of obtaining grid-independent solutions with respect to local details in the region of channels. Grid convergence patterns and numerical uncertainty are found to be dependent on the applied scheme. In general, the first-order hybrid scheme is diffusive and under predicts the formation of channels. The second-order central-difference scheme brings about oscillations with possible non-physical extremes of solute composition in the region of channel segregates due to sharp gradients in the solutal field. The results obtained using TVD and WENO schemes contain no oscillations and show an excellent capture of channels formation and resolution of the interface between solute-rich and depleted bands. Different stages of channels formation are followed by analyzing thermo-solutal convection and macrosegregation at different times during solidification.

Research limitations/implications – Accurate prediction of local variation in the solutal and flow fields in the channels regions requires grid refinement up to scales in the order of microscopic dendrite arm spacing. This imposes limitations in terms of large computational time and applicability of available macroscopic models based on classical volume-averaging techniques.

Practical implications – The present study is very useful for numerical simulation of macrosegregation during ingot casting of metal alloys.

Originality/value – The paper provides the methodology and application of TVD schemes to predict channel segregates during columnar solidification of metal alloys. It also demonstrates the limitations of classical schemes for simulation of alloy solidification.

Keywords Alloys, Flow, Solidification, Formed materials, Numerical analysis
Paper type Research paper

International Journal of Numerical Methods for Heat & Fluid Flow
Vol. 20 No. 8, 2010
pp. 841-866

0961-5539
DOI 10.1108/09615531011081405

Nomenclature

C_0	initial mass fraction of solute (Sn) in the alloy (wt%)
Cmax	maximum solute concentration (%)
Cmin	minimum solute concentration (%)
corr	correction term
c_p	specific heat ($J\,kg^{-1}\,K^{-1}$)
$\langle C \rangle$	average mass fraction of solute (Sn) (wt%)
D	solutal diffusion coefficient ($m^2\,s^{-1}$)
ERE	extrapolated relative error
f_{fine}	value of variable at the finest grid
f_{ext}	value of variable extrapolated to zero grid size
$\hat{f}$	numerical flux
g	gravity ($m\,s^{-2}$)
GCI	grid convergence index
GES	global extent of segregation
g_l	volume fraction of liquid
h	enthalpy ($J\,kg^{-1}$)
$\langle h \rangle$	average enthalpy ($J\,kg^{-1}$)
k	thermal conductivity ($W\,m^{-1}\,K^{-1}$)
K	permeability (m^2)
k_o	binary partition coefficient
L	latent heat of fusion ($J\,kg^{-1}$)
m_l	liquidus slope ($°C\,wt\%^{-1}$)
p	pressure (Pa)
Pe_T, Pe_D	Peclet Number for thermal and solutal transport ($Re_M\,Pr$ or $Re_D\,Sc$)
Pr	Prandtl number (ν/α)
Re_M	cell Reynolds number ($V\Delta x/\nu$)
S_c	source term
Sc	Schmidt number (ν/D)
t	time (s)
T	temperature (°C)
TV	total variation
v	superficial average velocity ($m\,s^{-1}$)
V	volume (m^3)
$\mathbf{v_l}$	intrinsic velocity of the liquid phase ($m\,s^{-1}$)
V_{domain}	volume of the computational domain (m^3)
w	nonlinear weights
X, Y	coordinate axes (m)

Greek symbols

$\gamma_i^{n,LW}$	Lax Wendroff slope, Eq. (18)
$\gamma_i^{n,T}$	limited slope
Δt	time step (s)
Δx, Δy	grid size (m)
β	smoothness indicators
β_T	thermal expansion coefficient ($°C^{-1}$)
β_c	solutal expansion coefficient ($wt\%^{-1}$)
λ_2	secondary dendrite arm spacing (m)
α	thermal diffusivity ($m^2\,s^{-1}$)
ν	kinematic viscosity ($m^2\,s^{-1}$)
μ	dynamic viscosity ($kg\,m^{-1}\,s^{-1}$)
σ	CFL number ($\sigma = \Delta t/\Delta x$)
ρ	mass density ($kg\,m^{-3}$)

Subscripts

l	Liquid
m	melting point for a pure substance
k	grid point
ref	reference conditions
s	solid

1. Introduction

Local variations of average solute mass fraction at the macroscopic scale of a casting are called macrosegregation. The most common cause of macrosegregation in ingots is fluid flow in the mushy zone induced due to variation of density with temperature and concentration which redistributes segregated solute elements within the remaining liquid volume. Thermo-solutal interactions in the mushy zone and at the solidification front in an ingot result in the formation of preferred flow channels. These channels are called A-segregates and result in the development of solute-rich bands adjacent to solute depleted bands in the final casting.

Macrosegregation is one of the major casting defects. Therefore, it has been extensively investigated with the help of mathematical models in the past. Reviews on the subject are available in the literature (Prescott and Incropera, 1996; Beckerman and Viskanta, 1993; Beckermann, 2002). Broadly, two types of models are employed in the study of macrosegregation: single-phase models and multi-phase models. In single-phase models, only one set of governing equations is used to describe the transport phenomena in the liquid, solid, and mushy regions. There are two basic formulations to arrive at a single-phase model:

(1) the continuum mixture method theory (Voller *et al.*, 1989; Bennon and Incropera, 1987; Prescott *et al.* 1991); and

(2) the volume-averaging technique (Ni and Beckermann, 1991; Ganesan and Poirier, 1990; Goyeau *et al.*, 2004).

While the mixture method is simple to work with, the volume-averaging method provides more insight into the physical basis of the process. It should be mentioned that the volume-averaging approach originally leads to a multi-phase model with separate equations for the liquid and solid phases that include appropriate interface transfer terms (Ni and Beckermann, 1991). However, a single-phase model can be obtained using the volume-averaging technique by adding up the resulting macroscopic conservation equations for the solid and liquid phases and making use of the interfacial balances (Ganesan and Poirier, 1990; Ni and Beckermann, 1991). Studies reported in the literature are concerned with the solidification of binary alloys and multi-component alloys (Prescott and Incropera, 1994; Schneider and Beckermann, 1995; Amberg, 1991; Felicelli *et al.,* 1991, 1997).

From these studies, it is evident that mathematical models, in general, have provided good insight into the formation of macrosegregation. However, the quantitative match between numerical prediction and experimental data is far from satisfactory. The previous numerical simulations of alloys solidification investigated the effects of one or more of the mechanisms leading to macrosegregation. However, rigorous verification procedure has not been demonstrated and no clear numerical reference solution exists in the literature. In order to reach a reference solution, the effect of discretization errors, i.e. numerical diffusion and dispersion, on the predictions is an important issue. The efforts to clarify some of the numerical issues were made by Venneker and Katgerman (2002) for direct chill casting. A potential source of errors lies in the transformation of governing differential equations to discretized equations. In this regard, incorrect treatment of the convection term can result in two types of errors: numerical diffusion (spreading out of profiles) and numerical dispersion (appearance of wiggles or oscillations) on the profile. Roughly speaking, numerical diffusion is common to first-order schemes when convection dominates diffusion (high cell-Peclet numbers). Numerical dispersion is common for unbounded high-order schemes and occurs in the vicinity of steep gradients.

Traditionally, the first-order upwind and power law schemes have been generally utilized in previous simulations of ingot solidification because of their simplicity and robustness in the sense that one can always get some output, although it may not be very accurate.

Complex flow structures associated with the development of flow channels and sharp gradients in the solutal field in the region of channels segregates call for the implementation of accurate methods for numerical modeling of alloy solidification. In particular, the solute transport equation is convection dominated and requires special non-oscillarity type high-order scheme to handle the regions of channel segregates. In recent years, high-order numerical methods have been widely used in computational fluid dynamics to effectively resolve complex flow features and treat such discontinuities. Such schemes come from the total variation diminishing (TVD) theory (see LeVeque, 1990). The non-oscillating property of a TVD scheme is obtained by limiting the conservative flux of a high-order scheme so as to check the TVD requirements as will be explained in section 2.

Weighted essentially non-oscillatory (WENO) schemes are designed based on the successful essentially non-oscillatory (ENO) schemes in Harten *et al.* (1987), Shu and Osher (1988) and Shu and Osher (1989). Both ENO and WENO use the idea of adaptive stencils in the reconstruction procedure based on the local smoothness of the numerical solution to automatically achieve high-order accuracy and non-oscillatory property near discontinuities. ENO uses just one (optimal in some sense) out of many candidate stencils when doing the reconstruction; while WENO uses a convex combination of all the candidate stencils, each being assigned a non-linear weight which depends on the local smoothness of the numerical solution based on that stencil. WENO improves upon ENO in robustness, better smoothness of fluxes, better steady state convergence, better provable convergence properties, and more efficiency. For more details of ENO and WENO schemes, we refer to Jiang and Shu (1996) and Shu (2003).

The TVD property is a global property of an advection scheme. It goes some way toward preventing spurious amplification of extrema. High-resolution schemes based on the TVD theory have been used in other domains to resolve problems involving strong convection and discontinuities in the solution field (Harten, 1983; Sweby, 1985; Wang and Hutter, 2001). Surprisingly, so far, in numerical modeling of thermo-solutal convection and solidification of alloys, only few models use high-resolution schemes to simulate convection terms. However, high-order methods have been extensively used in simulation of dendritic microstructure during crystallization (Gibou *et al.*, 2003). In the present article, special attention is given to the numerical treatment of solute transport equation. Numerical discretization of solute transport equation using hybrid or central-difference schemes follows the classical procedure. Application of special non-oscillarity type high-order schemes that are based on the TVD theory to the solute transport equation requires special treatment. A two-step time-splitting procedure has been adopted to handle the solute transport equation. In the first step, the advection part of solute transport, hyperbolic equation, is explicitly treated using high-order TVD schemes. In the second step, the contribution of solute diffusion and source terms are implicitly treated. Up to the authors' knowledge, the concept of time splitting of concentration equation and application of high-order TVD schemes for solidification modeling have not been addressed in the literature. In the present study, we report on the application of explicit-splitting Lax-Wendroff TVD SUPERBEE scheme (Vincent and Caltagirone, 1999) and the fifth-order WENO scheme (Jiang and Shu, 1996) using the third-order Runge-Kutta method for time discretization. We consider solidification

of a binary Pb-18%Sn alloy in a two-dimensional rectangular domain for analysis of therm-osolutal convection, channels formation, and macrosegregation fields obtained using different numerical approaches. The governing equations for mass, momentum, energy, and species are based on the volume-averaging method (Ganesan and Poirier, 1990; Ni and Beckermann, 1991; Rappaz *et al.*, 2003; Goyeau *et al.*, 2004). Numerical simulations have been carried out using different grid sizes to study the convergence behavior and numerical uncertainty using different schemes. Different stages of channels formation are followed by analyzing thermo-solutal convection and macrosegregation at different times during solidification.

2. Physical model

We consider solidification of a binary Pb-18%Sn alloy in a two-dimensional rectangular domain of height H and width W as shown in Figure 1. The thermo-physical properties of Pb-18%Sn are listed in Table I. Initially, the liquid alloy is stagnant at a uniform temperature T_o and concentration C_o. At time $t = 0$, solidification starts by cooling the left and right walls with an external cooling fluid of temperature (T_{ext}) and an overall heat transfer coefficient (U). The two other sides of the cavity are insulated. A solid phase and a mushy layer then grow from the cold boundaries, and convective motions driven by both thermal and solutal buoyancy can occur. A rigid and connected solid phase is assumed, which forms a porous mush in the phase change zone. To keep the problem simple, we suppose that the solid and the liquid have the same density, the Boussinesq approximation is valid, and macroscopic species diffusion in the solid phase is neglected as compared to macroscopic solute diffusion in the liquid phase ($D_s \ll D_l$). Besides, we suppose that the permeability is given by the Carman-Kozeny function with a fixed secondary dendrite arm spacing, λ_2:

$$K = \frac{\lambda_2^2 g_l^3}{180\,(1 - g_l)^2} \tag{1}$$

The macroscopic conservation equations based on the volume-averaging method consist of transport equations for mass, momentum, heat, and species, simultaneously valid in the liquid, mushy, and solid regions. They are written as (Ganesan and Poirier, 1990;

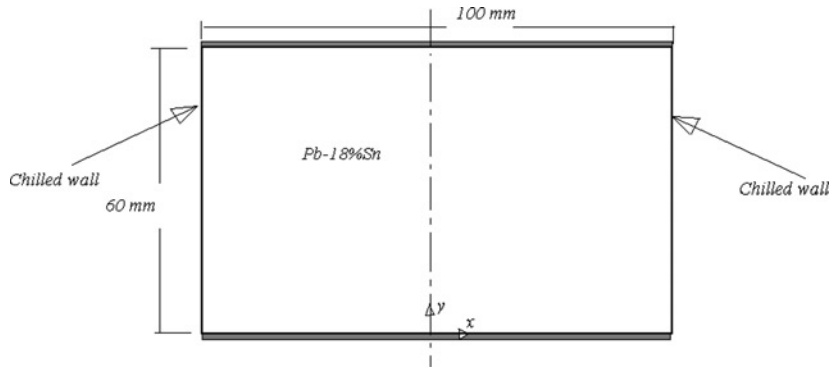

Figure 1.
Physical model, solidification of Pb-18%Sn in a rectangular cavity

Property	Symbol	Units	Pb-18%Sn
Specific heat	c_p	$\mathrm{J\,(kg\,K)^{-1}}$	176
Latent heat of fusion	L	$\mathrm{J\,kg^{-1}}$	3.76E+04
Thermal conductivity	K	$\mathrm{W\,(m\,K)^{-1}}$	17.9
Liquid dynamic viscosity	M	Pa s	1.10E−03
Secondary dendrite arm spacing	Λ_2	m	1.85E−04
Liquid thermal expansion coefficient	β_T	$\mathrm{K^{-1}}$	1.16E−04
Liquid solutal expansion coefficient	β_C	$\mathrm{(wt\%)^{-1}}$	4.90E−03
Nominal concentration	C_o	wt%	18.0
Reference density	ρ_o	$\mathrm{kg\,m^{-3}}$	9250
Melting point at $C = 0$	T_p	°C	327.5
Eutectic temperature	T_e	°C	183.0
Eutectic composition	C_{eut}	wt%	61.911
Equilibrium partition coefficient	K_o		0.310
Liquidus slope	m_l	$\mathrm{°C\,(wt\%)^{-1}}$	−2.334
Liquidus at nominal concentration	(T_{liq})	°C	285.488
Diffusion coefficient in the liquid	D_l	$\mathrm{m^2\,s^{-1}}$	1E-9
Heat transfer coefficient	U	$\mathrm{W\,m^{-2}K^{-1}}$	400
External temperature	T_{ext}	°C	25

Table I.
Physical properties of Pb-18%Sn

Ni and Beckermann, 1991; Rappaz *et al.*, 2003):

$$\nabla \cdot \mathbf{V} = 0 \tag{2}$$

$$\nabla \cdot (\mu_l \nabla \mathbf{V}) - g_l \nabla p - \frac{\mu_l g_l}{\mathrm{K}} \mathbf{V} + g_l \tilde{\rho} \mathbf{g} = \rho \frac{\partial \mathbf{V}}{\partial t} + \frac{\rho}{g_l} \mathbf{V} \cdot (\nabla \mathbf{V}) \tag{3}$$

$$\rho \frac{\partial \langle h \rangle}{\partial t} + \rho c_p \nabla T \cdot \mathbf{V} - \nabla \cdot (k \nabla T) = 0 \tag{4}$$

$$\frac{\partial \langle C \rangle}{\partial t} + \nabla C_l \cdot \mathbf{V} = \nabla \cdot (D_l \nabla C_l) \tag{5}$$

where $\mathbf{V} = g_l \mathbf{v}_l, \mathbf{v}_s = 0, p = p_l$, $T_s = T_l = T$, $k_s = k_l = k$, $\rho_s = \rho_l = \rho$, $c_{ps} = c_{pl} = c_p$, $g_s + g_l = 1$, and μ_l is considered constant. g_s and g_l denote the volume fractions for solid and liquid phases. Expression of specific enthalpy for solid (h_s) and liquid (h_l) phases, and of the average specific enthalpy $\langle h \rangle$ are written as:

$$h_s = c_p T, \quad h_l = c_p T + L, \quad \langle h \rangle = c_p T + g_l L \tag{6}$$

With L denoting the specific latent heat, supposed constant. The variation of density with temperature and concentration is calculated using:

$$\tilde{\rho} = \rho_o \big(1 - \beta_T (T - T_{ref}) - \beta_C (C_l - C_{ref})\big) \tag{7}$$

where

$$\beta_T = -\frac{1}{\rho}\left(\frac{\partial \rho}{\partial T}\right)_P, \quad \beta_C = -\frac{1}{\rho}\left(\frac{\partial \rho}{\partial C}\right)_P, \quad T_{ref} = T_p + m_l C_0, \quad \text{and} \quad C_{ref} = C_0.$$

With $T_{ref} = T_p + m_l C_0$, where T_p is the melting temperature at zero concentration, m_l is the slope of the liquidus line, $C_{ref} = C_0$ (nominal mass concentration of solute in the binary alloy), β_T the constant volumetric thermal expansion coefficient, and β_C the constant volumetric solutal expansion coefficient.

3. Coupling procedure

The temperature-solute coupling problem is closed on specifying the thermodynamics and the local scale transport behavior. The condition of thermodynamic equilibrium at the solid-liquid interface, $C_s = k_o C_l$, suggests that the liquidus line in the phase diagram can be used to specify a relationship between the liquid concentrations and the temperature. For a linearized liquidus line of a binary alloy system this relationship is given by:

$$T = T_p + m_l C_l \tag{8}$$

C_l and C_s are the intrinsic phase-averaged mass concentration of solute in the liquid and solid phases. k_0 is the partition coefficient.

A central step in the coupling of the solute and temperature is the correct accounting of the local scale (microscopic) mass diffusion that occurs in the dendritic arm spaces. When specifying the liquid fraction, g_l, and solute density, $\langle C \rangle$, the requirement is to obtain a value for the REV liquid concentration, C_l. The value of C_l is controlled by the microscopic solute diffusion of the solute in the solid phase, often referred to as "back diffusion." In the simple case of complete microscopic solute diffusion in the solid and liquid phases, local thermodynamic equilibrium is achieved and the lever rule can be used to obtain C_l:

$$C_l = \frac{\langle C \rangle}{k_o + g_l(1 - k_o)} \tag{9}$$

In the general case, however, back diffusion is finite and a more detailed treatment of the local scale transport process is required.

Solutions of macroscopic conservation equations of momentum, energy and solute transport are carried out using the most recent available values of g_l and C_l. Special procedure is required to handle the energy equation and calculate the liquid fraction g_l. An inner iteration is performed that adjusts the nodal temperature field and calculates the current liquid fraction g_l. The objective of this inner iteration is to find nodal fields that simultaneously satisfy the constraint equations (Equations (8) and (9)). This inner iteration is a key step in this coupling approach. The current iterate of the liquid fraction $(i + 1)$ can be approximated as function of the previous one (i) as:

$$g_l^{i+1} = g_l^i + corr \tag{10}$$

At convergence, the value of correction "corr" is zero. In fact, the correction term is driven by the difference between the temperature resulting from the present iteration of energy equation and the liquidus temperature driving the phase change process along the liquidus line. Therefore, the value of "corr" can be written in a general way in the form:

$$corr = \frac{c_p(T - T_{liq})}{L} \tag{11}$$

where T_{liq} is a function of solute concentration in the liquid given by Equation (8).

The advantage of this technique is that at convergence the temperature at any point in the mushy zone corresponds to the equilibrium temperature as determined by the equilibrium phase diagram. No supplementary corrections are needed for the temperature field provided that the liquid fraction field is correct (corr = zero).

The present simple coupling algorithm can be summarized as follows:

- Starting with the initial guesses (or variable initialization);
- Solve the momentum equation;
- Solve the energy equation;
- Correct liquid fraction using Equation (10), and solve energy equation until convergence of liquid fraction field (corr < 1E − 7);
- Solve solute transport equation; and
- Advance time, reinitialize variables and restart calculation.

In this simple coupling approach, the time step is assumed to be sufficiently small so that the effect of variation in solute concentration on the liquidus temperature is negligible. Therefore, the inner iteration loop of energy equation uses the last available value of C_l. During solution, values of the residuals of momentum, energy, and species equations less than 10^{-15} are assured to obtain a converged solution. The total mass imbalance ($\nabla . V$) is less than 10^{-8}.

4. Numerical solution of solute transport

Traditionally, first-order numerical methods are often used in numerical simulations of alloy solidification. However, it is well known that the flow structures during solidification are so complicated and the evolution time of these structures is long. Therefore, it is impractical to use low-order methods to obtain an acceptable resolution. This calls for the application of special non-oscillatory type high-order schemes, which are emphasized in this paper. Special attention is given to the solute transport equation, Equation (5), that is written in a form amenable to numerical solution as:

$$\frac{\partial \langle C \rangle}{\partial t} + \nabla \langle C \rangle \cdot V = \nabla . (D_l \nabla C_l) + S_c \tag{12}$$

where $S_c = \nabla(\langle C \rangle - C_l) \cdot V$.

Since the diffusion coefficient of solute in the liquid phase is usually very small ($D_l = 10^{-9}\,m^2 s$), Equation (12) is convection dominated (nearly hyperbolic). Also, the existence of high gradient regions (channel segregates) in the solution makes it difficult to obtain accurate numerical solutions using classical numerical schemes. The classic schemes do not offer good enough results: a first-order upwind scheme is too diffusive and a high-order scheme (such as central difference, Lax-Wendroff, and Quick) brings about oscillations due to sharp gradients in the composition field. As a consequence, these types of schemes do not ensure a precise calculation of the interfaces associated with the area of channel segregates. A good way of solving Equation (12) is to apply methods used in compressible fluid mechanics to solve hyperbolic conservation laws. Hyperbolic problems are characterized by the existence of discontinuities spreading or appearing during the evolution. This property requires the use of a robust scheme able to be applied in the presence of discontinuities. We also want a high-order scheme giving accurate solutions. Such schemes are derived from the TVD theory (see LeVeque, 1990).

A desirable property of an advection scheme is that it should be "monotonicity-preserving" or "shape-preserving"; that is, it should not create spurious extrema or cause spurious amplification of existing extrema in an advected quantity. This desirable property can be achieved by carefully constraining or "limiting" the advective fluxes calculated by the scheme. Consider the advection of solute concentration C in one dimension by a velocity u, described by the equation:

$$\frac{\partial C}{\partial t} + u\frac{\partial C}{\partial x} = 0 \tag{13}$$

and, to simplify the discussion, restrict our attention to the case where u is constant and positive. Let C_k^n be a discrete approximation to C in the k^{th} grid box at time step n. The total variation TV at time step n is defined as:

$$TV^n = \sum_k |C_{k+1}^n - C_k^n| \tag{14}$$

A scheme is TVD if it ensures that $TV^{n+1} \leq TV^n$.

Many high-order methods are used in CFD, suitable for solving hyperbolic conservation law, such as the compressible Euler equation, or convection-dominated convection-diffusion problem, such as the compressible Navier-Stokes equations, at high Reynolds numbers. For such problems, shocks and other discontinuities or high gradient regions exist in the solutions, making it difficult to design stable and high-order numerical methods. We have decided to apply the TVD theory (LeVeque, 1990; Yee, 1987; Hirsch, 1990) to the equation of solute transport. An explicit-splitting Lax-Wendroff TVD SUPERBEE scheme (Vincent and Caltagirone, 1999) is adopted. The obtained scheme is of second order, except near the discontinuities, where a first order is enforced. Also, an implementation of fifth-order WENO scheme that follows the description of Jiang and Shu (1996) using third-order Runge-Kutta method for time discretization is carried out. A first-order hybrid scheme and a second-order central-difference scheme are also employed for the purpose of comparisons. Numerical discretization of solute transport equation using hybrid or central-difference schemes follows the classical procedure and shall not be repeated here.

Application of special non-oscillarity type high-order schemes that are based on the TVD theory to the solute transport equation requires special treatment. In the present study, a two-step time-splitting procedure has been adopted to handle the solute transport equation. In the first step, the advection part of solute transport, hyperbolic equation, is explicitly treated using high-order Lax-Wendroff TVD SUPERBEE or WENO schemes by considering the system:

$$\frac{C^* - C^n}{\Delta t} + \nabla C^n . V = 0 \tag{15}$$

In the second step, the contribution of solute diffusion and source terms are implicitly treated by considering the system:

$$\frac{C^{n+1} - C^*}{\Delta t} = \nabla .(D_l \nabla C_l^{n+1}) + S_c^{n+1} \tag{16}$$

The final result is equivalent to solving the complete system given by:

$$\frac{C^{n+1} - C^n}{\Delta t} + \nabla C^n . V = \nabla . (D_l \nabla C_l^{n+1}) + S_c^{n+1} \tag{17}$$

The details of Lax-Wendroff TVD SUPERBEE second-order scheme, WENO fifth-order scheme, and their numerical implementations are briefly outlined in the appendix.

5. Solution methodology

The governing equations are discretized using the finite-volume method on a staggered unique mesh. The resulting linear systems of equations are solved using MUltifrontal Massively Parallel sparse direct Solver. An augmented lagrangian method is used to handle the velocity-pressure coupling. The augmented-lagrangian method allows to decouple the fields of pressure and velocity (Fortin and Glowinski, 1982). This predictor/corrector iterative method consists of solving an optimization problem by solving a velocity-pressure saddle point with an Uzawa algorithm. It is an iterative method which consists, starting from an initial field of pressure, of solving the NS equations modified by the introduction of the constraint of divergence null, then calculating a new field of pressure using a modified continuity equation. A central-difference convection scheme is used for the discretization of energy and momentum equations. The utilization of central-difference scheme for energy and momentum equations will be justified in the next section. Different schemes have been utilized for the solute transport equation as described above.

6. Results and discussion

Comparisons of numerical results using hybrid, central difference, TVD, and WENO schemes are presented in the following sections. The ultimate purpose is to present grid independent results. However, as will be shown below, the results of numerical simulations show the difficulty of obtaining grid-independent solutions with respect to channels formations because of the highly unstable and transient convection phenomena and the physics associated with channels development. Therefore, an analysis of grid convergence rates and numerical uncertainty using different schemes are performed first to decide the selected grid for final presentation of results. Comparisons of flow, temperature, solid fraction, and global macrosegregation fields are then discussed using solutions obtained at the finest grid. The interest here is to compare the results obtained using different schemes. The issue of obtaining a reference solution is addressed in terms of required computational time and the need for parallel computations.

6.1 Grid convergence and numerical uncertainty

The assessment of numerical uncertainty is necessary for verification of CFD codes to become a reliable tool for the analysis and design (Oberkampf and Trucano, 2008). A potential source of errors lies in the transformation of governing differential equations to discretized equations. The approach of calculation verification involves performing a grid convergence study and determining the observed order of convergence, error bands, and grid convergence indices. Previous numerical simulations of alloys solidification have concentrated on the effects of one or more of the mechanisms leading to macrosegregation. Little attention is devoted to demonstrate rigorous verification procedure. One major difficulty of the present analysis lies in the choice of appropriate variables for assessment of grid convergence and estimation of numerical

uncertainty. Since macrosegregation is the ultimate concern in simulation of alloy solidification, parameters related to final solute segregation at the end of solidification are adopted as quantitative measures for grid convergence study. A global extent of segregation (GES) is calculated as (Schneider and Beckermann, 1995):

$$GES\% = \frac{100}{C_o}\left[\frac{1}{V_{domain}}\iiint_{Vdomain}(C - C_o)^2 dv\right]^{1/2} \tag{18}$$

The GES takes the general form of standard deviation. Thus, a large value of GES indicates that the data points are far from the mean (high segregation) and a small value of GES indicates that they are clustered closely around the mean (low segregation). The values of relative deviation of minimum and maximum concentration from the average initial value, $Cmin\% = 100(C_{min} - C_o)/C_o$ and $Cmax\% = 100(C_{max} - C_o)/C_o$, are adopted as local measures for the intensity of macrosegregation. In addition, final macrosegregation patterns showing the percentage relative deviation of concentration from the average, $100(C_i - C_o)/C_o$, are plotted and compared for different grids.

Many of the approaches proposed in the literature for quantification of the numerical uncertainty are based on grid refinement in conjunction with Richardson extrapolation (RE) (Roache, 1998). RE usually uses calculations on three grids to determine the extrapolated value of a dependent variable to zero grid size, either using the theoretical order of the scheme (on at least two grid levels), or via the apparent or observed order which is calculated as part of the solution. In spite of being a very useful tool for quantifying discretization errors in CFD, there still remain major problems that need to be addressed to advance the level of confidence that could be trusted upon RE. Alternative methods are proposed due to the difficulties of RE (Celik and Li, 2005). These techniques estimate the numerical uncertainty based on the difference between the computed solution and a higher-order reconstruction obtained using appropriate non-linear extrapolation methods using a minimum of five grids. Assuming the grid size as Δx or Δy, the extrapolated variable of interest is defined as $f_{ext} = f_{\Delta x=0}$. In the present study, a uniform grid with $\Delta x = \Delta y$ is used and a cubic-spline method is adopted for extrapolation of computed quantities. Once f_{ext} is known the numerical uncertainty is calculated using the fine grid convergence index proposed by Roache (1998) which is written in terms of solution obtained at the fine grid f_{fine} as:

$$GCI_{fine} = F_s\left|\frac{f_{ext} - f_{fine}}{f_{fine}}\right| \tag{19}$$

The GCI indicates an error band on how far the solution is from the asymptotic value. It indicates how much the solution would change with a further refinement of the grid. The factor of safety is recommended to be $F_s = 3.0$ for comparisons of two grids and $F_s = 1.25$ for comparisons over three or more grids. The extrapolated relative error (ERE) can be also used to quantify the uncertainty which is defined as (Celik and Li, 2005):

$$ERE = \left|\frac{f_{ext} - f_f}{f_{ext}}\right| \tag{20}$$

Numerical simulations have been carried out using different schemes for five different values of uniform grid sizes. Referring to a given grid size by the subscript n, the grid

refinement ratio is defined as $r = \Delta x_n/\Delta x_{n-1}$. The value of r is taken to be constant and equal to 1.4. The first grid used (50×60) corresponds to a value of $\Delta x = \Delta y = 0.001$ m and is referred to as $k = 0$, i.e. $\Delta x = \Delta x_o$.

The convergence patterns using different schemes are shown in Figure 2 for the calculated values of Cmin%, Cmax%, and GES. These are represented as function of the normalized grid spacing defined as $\Delta x_n/\Delta x_o$. Two types of grid convergence can be identified, namely monotonic and non-monotonic. A convergence is defined to be monotonic whenever the product $(f_n - f_{n-1})(f_{n+1} - f_n)$ is less than zero for any grid index n (Celik and Li, 2005). Monotonic convergence patterns are observed for hybrid, TVD, and WENO schemes for the three measures of Cmin%, Cmax%, and GES. The convergence patterns using central-difference scheme are non-monotonic. As compared to other schemes, lower values of Cmin% and higher values of Cmax% are obtained using the central-difference scheme. The values of Cmax% obtained using the hybrid scheme are relatively lower than those obtained using other schemes. Using hybrid, TVD, and WENO schemes, a remarkable increasing tendency of Cmax% and low decreasing tendency of Cmin% are obtained with refining the grid. Using the central-difference scheme, some unrealistic values of Cmin% and Cmax% outside the range of theoretical expected limits of Cmin% $= -69.30$ percent, Cmax% $= 243.95$ percent are observed. These theoretical limits correspond to the ultimate cases of instant solidification of initial liquid of composition C_o, resulting in a solid with concentration $C_s = k_o C_o$ and the maximum possible eutectic composition of C_{eut}. The unrealistic Cmin% values are only noted while using coarse grids. However, the unrealistic value of Cmax% is obtained using fine grid of 192×231. This observation is important as it points to the possibility of wrong prediction of eutectic formation using the CD scheme. Concerning GES, it can be observed that the values obtained using the hybrid scheme are always lower than other schemes. Comparable values of GES are obtained using TVD and WENO schemes. Slightly higher values of GES are obtained using the central-difference scheme.

One may conclude that, in terms of Cmin%, and Cmax%, the results are far from grid independent. However, the numerical uncertainty in the calculation of Cmin% and Cmax% should be analyzed by considering the areas associated with each of them as will be discussed later using macrosegregation maps. In terms of GES, one has to note that the changes over the span of scale depicted in Figure 2(a) are small. An analysis of numerical uncertainty in the calculated GES is shown in Table II for grid of 192×132. Values of GCI and ERE are acceptable. The hybrid scheme show relatively high values of GCI and ERE.

The behavior of variation of Cmin% with grid refinement using WENO and TVD schemes shows two important stages of grid dependence. In the first stage, Cmin% shows small variation with grid refinement, grid refinement improves the overall prediction of channels formation in terms of location and number. In the second stage, Cmin% starts to decrease relatively faster, further grid refinement better resolves the local details of flow within channels. Increasing the number of nodal points within a channel increases the predicted intensity of flow passing through the channel, as will be shown later. The enrichment of solute within a channel comes at the expense of adjacent areas that are depleted from solute. Therefore, the value of Cmin% starts decreasing with the increasing the number of nodal points.

Note that, the present computations have not reached a reference grid-independent solution. The required CPU computational time is very high. For example using 268×324 grid, the CPU computation time is about 4 h for each second of process time,

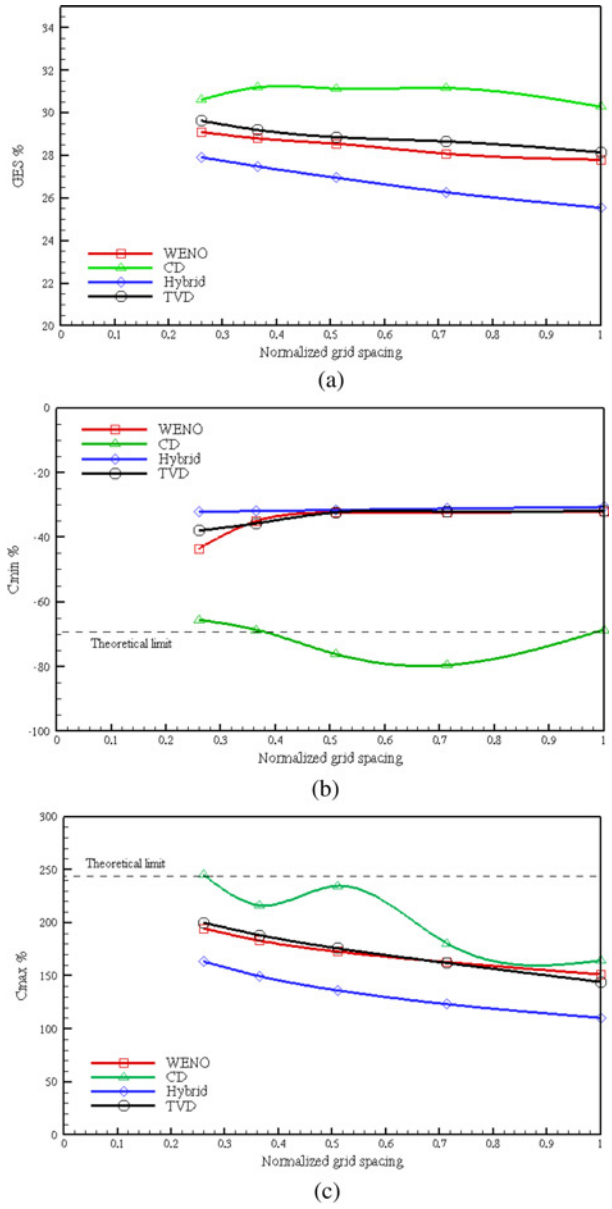

Notes: (a) GES; (b) Cmin%; (c) Cmax%

Figure 2.
Variation of GES, Cmin%, and Cmax% with grid size

using a time step of 0.001 s. In view of the total solidification time (460 s), this required 76 days of CPU time on SGI Altix ICE 8200 Supercomputer (three Tflops, 32 computation nodes, total of 256 Intel Xeon quad-core processors 3 GHZ, memory 2 G/core, total memory 0.5 T) for which parallel computation would be useful.

6.2 Macrosegregation patterns

The above analysis has considered only comparisons of quantitative measures of macrosegregation. Further investigations have been carried out to compare the final macrosegregation patterns predicted using different schemes and their variation with mesh size. Macrosegregation patterns obtained using different schemes are shown in Figures 3-6. They are all drawn between minimum and maximum values of −80 and 250 percent using 10 percent as an interval. The selected range of these levels exceeds the theoretical limits of Cmin% and Cmax% discussed above. It was dictated by the values of Cmin% and Cmax% obtained using the central-difference scheme, see Figure 2. The interest is to give a unified picture for proper comparison of different schemes. For clearness, the values of Cmin% and Cmax% are noted on the top of each figure. In all figures the areas of maximum solute concentration (Cmax%) are observed to be associated with the channel formed at the top of the cavity. On the other hand, the values of minimum solute concentration (Cmin%) are found to exist in the solute depleted bands adjoining each channel in the upper right corner of the cavity. As can be inferred from the maps, the percentage of these areas to the total cavity area is very small.

Table II.
Numerical uncertainty in GES% using different schemes for 192 × 231 grid

Scheme	GES extrapolated to h = 0	GES at finest grid	GCI%	ERE%
WENO	29.449	29.104	1.480	1.184
CD	31.046	30.602	1.813	1.451
HYBRID	28.865	27.917	4.245	3.396
TVD	30.255	29.628	2.645	2.116

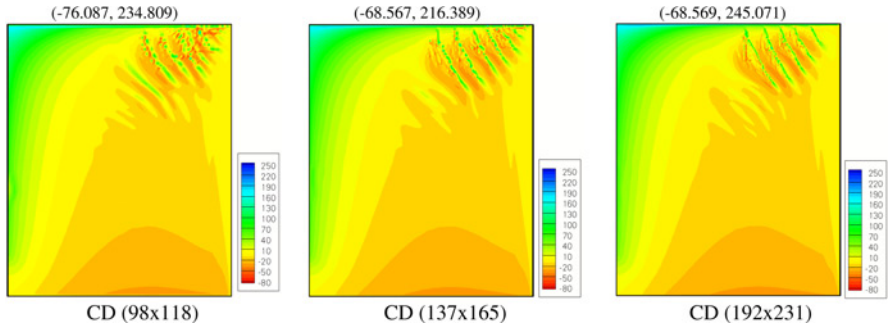

Figure 3.
Macrosegregation patterns obtained using CD scheme for different grid sizes

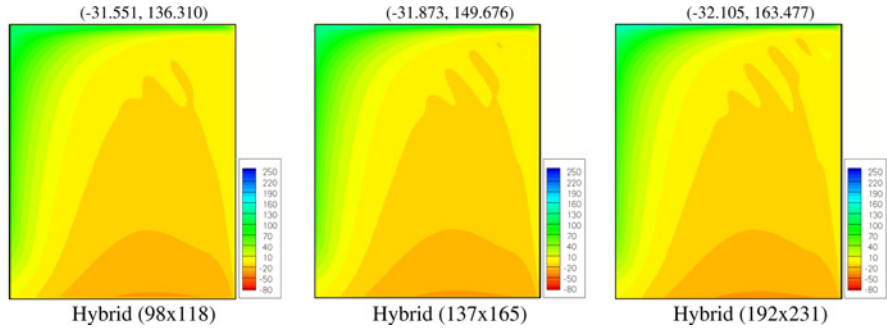

Figure 4.
Macrosegregation patterns obtained using hybrid scheme for different grid sizes

In general, using WENO and TVD schemes, the number of channels increases with refinement of the grid. For 192 × 231 and finer grids, the number of channels does not change with grid refinement. However, the local variations in the area of channels continue to change with further grid refinement. As compared to WENO scheme, less number of nodes is needed for the TVD scheme to predict the final number of channels. This may offer a computational time advantage for the use of TVD scheme.

On the other hand, the hybrid scheme fails to predict any channels even for the finest mesh of 192 × 231. Only the tendency to form channels is observed using hybrid scheme at 192 × 231. It seems that perturbations in the flow field which are in the general form of oblique flow at the region of channel formation, as will be discussed in detail in the following section, are damped by excessive false diffusion of the hybrid scheme. Moreover, channel segregates in the upper portion of the cavity are always oblique. They form what is known as "A" segregates in industrial ingots when one considers the complete cavity. It is well known that false diffusion associated with first-order schemes is non-negligible when the flow field is oblique to the grid boundaries.

In the present study, using CD scheme for simulations of channels development, it can be observed from Figure 3 that, in addition to unrealistic values of minimum and maximum solute concentration predicted by the CD scheme, the region of channels is characterized by highly non-uniform and sometimes ruptured interfaces between the solute-rich and solute depleted bands. The form of channels improves with the increase of number of nodes. However, the quality of channel shape is low as compared to the shape predicted using WENO and TVD schemes. The reason for this is that the second-order central-difference scheme brings about oscillations with non-physical extremes of solute composition in the region of channel segregates due to discontinuities in the

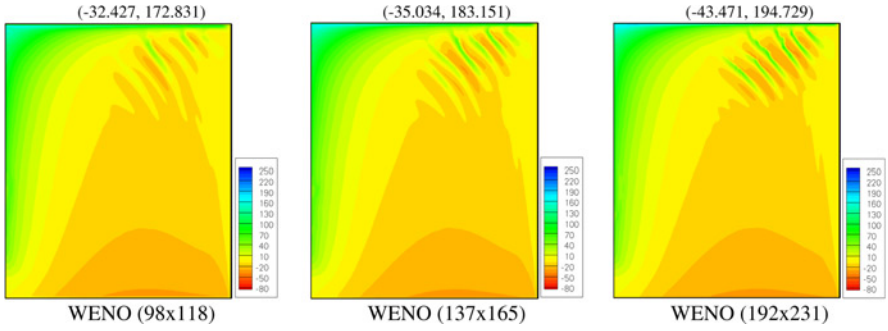

Figure 5.
Macrosegregation patterns obtained using WENO scheme for different grid sizes

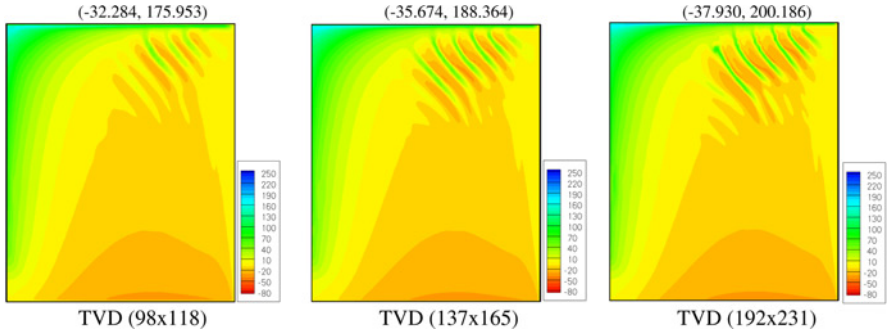

Figure 6.
Macrosegregation patterns obtained using TVD scheme for different grid sizes

solutal field. These oscillations can be clearly shown by investigating the horizontal concentration profile in the upper portion of the cavity (y = 50 mm) shown in Figure 7. Also, the number of channels predicted using the CD scheme is less than those obtained using TVD and WENO schemes.

To summarize, the first-order scheme suffers from numerical diffusion and the CD scheme suffers from numerical dispersion. Numerical diffusion is common to first-order schemes when convection dominates physical diffusion. Numerical dispersion is common for unbounded high-order schemes and occurs in the vicinity of steep gradients. Also, for CD scheme numerical oscillations increase when the value of cell Peclet number exceeds two. The relative importance of advection and diffusion is estimated based on the cell Peclet number. For diffusion of temperature (thermal diffusion), the cell Peclet number is defined as $Pe_T = V\Delta x/\alpha$. For mass diffusion, it is defined as $Pe_D = V\Delta x/D$, where V is the velocity and Δx is the cell size. For momentum transport a cell Reynolds number defined as $Re_M = V\Delta x/\nu$ is used. It should be noted that $Pe_T = Re_M.Pr$ and $Pe_D = Re_M.Sc$. An analysis of these values for different grids is shown in Table III. The value of velocity observed inside a channel is in the order of 0.001-0.003 m s^{-1}. Using a value of V = 0.002 m s^{-1} in the estimation of cell Reynolds and Peclet numbers, it is clear that the cell solutal Peclet number is very high. High values of cell solutal Peclet number and oblique flow inside a channel excludes the application of first-order and CD schemes for resolving solute-transport during solidification of alloys. In principle, grid refinement can alleviate these numerical errors. However, the degree of refinement is often totally impractical for engineering purposes. The adoption of such schemes includes the

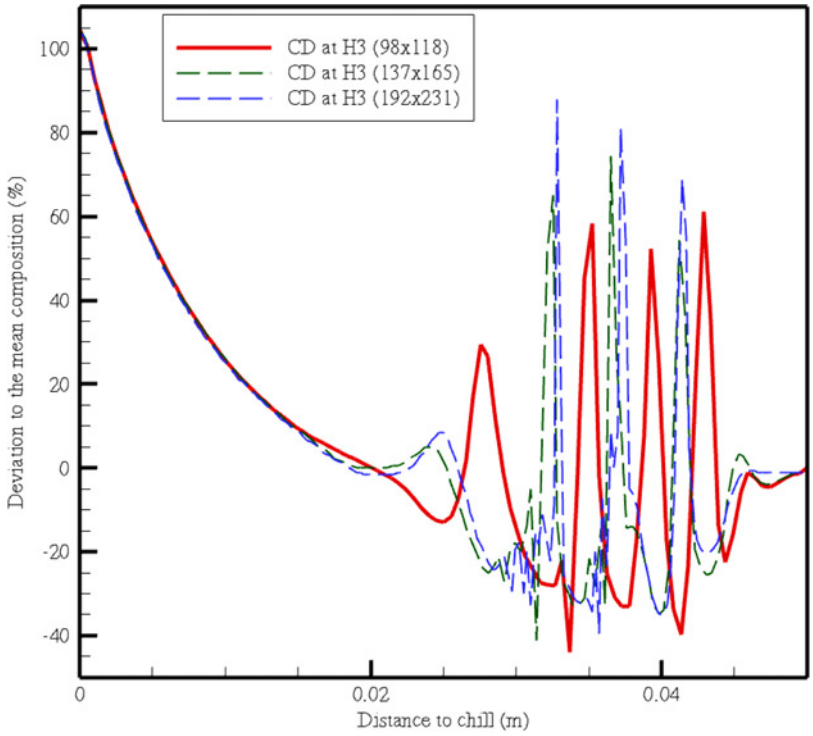

Notes: H3 at y = 50 mm

Figure 7.
Horizontal profile of mixture composition at the end of solidification using CD scheme for different grid sizes

challenges of eliminating numerical errors as well as describing local phenomena occurring in the channel region.

The Peclet number for solute transport is very high as due to very small value of solute diffusion coefficient. For momentum and energy transport, small values of cell Reynolds and Peclet numbers might allow the utilization of CD scheme. However, caution should be always taken regarding first-order schemes because of inherent numerical diffusion associated with oblique flow to grid boundaries. Previous studies reported by Mohamad and Viskanta (1989), Zhou and Zebib (1992), and Cless and Prescott (1996) also confirmed the unability of first-order schemes for predicting oscillatory convection in low Prandtl number natural convection. The second-order central-difference scheme was recommended for use in their transient simulations of low Pr natural convection.

The results obtained using TVD and WENO schemes contain no oscillations and show an excellent capture of channels formation and resolution of the interface between solute-rich and depleted bands. Apart from the channels region, the predicted macrosegregation in the other areas of the cavity using different schemes are approximately similar. This can be attributed as due to the absence of significant concentration gradients in these regions.

Using WENO and TVD schemes, the predicted channel width using 137 × 165 and 192 × 231 grids is about 1,000 μm. The value of mesh element is about 365 and 255 μm, respectively. That is we have about three nodes in the channel using 137 × 165 grid and four nodes using 192 × 231 grid. That is the grid length scale is sufficiently smaller than the channel width. This number of nodes can be considered as the minimum required for resolving the flow characteristics and following the stages of development of channels (to be discussed in the next section). Since channel size is related to the value of dendrite arm spacing ($d_2 = 185$ μm in the present study), we can say that the grid size should be in the order of dendrite arm spacing in order to accurately predict channels formations. In areas away from the channels region the grid size is not critical and a coarser mesh can be used. However, considerable differences between the various simulations that are apparent on the local scale, in particular in the region of channels formation, as noted in the variations of Cmax% and Cmin% for example, indicate that the minimum spacing recommendation is not sufficient to achieve grid-independent results. These differences are caused primarily by the highly unstable and transient convection phenomena associated with channels initiation and development. In addition, the local scale phenomena in the channels region are better described by the increasing the number of nodes in the channel.

As an example, Figure 8 shows the results obtained using WENO scheme employing further grid refinement. Results obtained using 192 × 231 and 268 × 324 are compared with a zoom on the channels region, where some local differences are noted by increasing the number of nodes within one channel from four to six. The flow structure in the channels region, represented by streamlines after 60 s of the beginning of cooling, changes with the increase of number of nodes in a single channel. It can be observed that,

Grid	Cell size (m)	Re_M	Pe_T	Pe_D
50 × 60	1.00E-03	1.68E+01	1.82E-01	2.00E+03
70 × 84	7.14E-04	1.20E+01	1.30E-01	1.43E+03
98 × 118	5.10E-04	8.58E+00	9.28E-02	1.02E+03
137 × 165	3.65E-04	6.14E+00	6.64E-02	7.30E+02
192 × 231	2.60E-04	4.38E+00	4.74E-02	5.21E+02
268 × 324	1.87E-04	3.14E+00	3.39E-02	3.73E+02

Table III. Values of cell Reynolds and Peclet numbers for different cell sizes

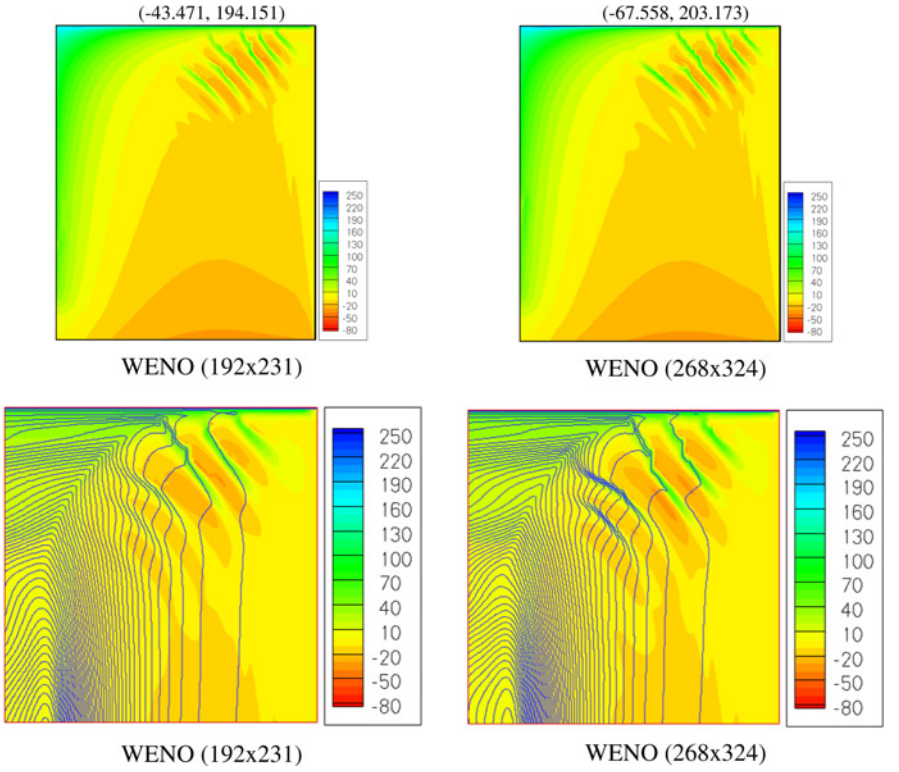

Figure 8.
Final macrosegregation pattern and zoom on the flow structure in the channels region after 60 s of cooling using WENO scheme with four and six nodes in a single channel

as compared to small number of nodes, the intensity of flow in a single channel increases. This can be inferred by closer spaced streamlines. This ultimately results in the increase of value of Cmax% and decrease in the value of Cmin% with the grid refinement.

6.3 Stages of development of channels segregates

In the present section the results obtained using 192 × 231 grid are analyzed to get further insight into the stages of development of channels and differences between TVD and CD schemes. For this purpose, we make a zoom on the upper right corner of the cavity and follow the development of channels by analyzing solute segregation and flow field represented by equally spaced streamlines, see Figure 9 for results obtained using TVD scheme and Figure 10 for results obtained using CD scheme. Also shown in Figures 9 and 10 the progress of liquidus front (represented by the isoline of $g_l = 0.95$) with time.

In the absence of liquid superheat, solutally driven circulation is dominant from the beginning of cooling. Sn-rich interdendritic fluid penetrates the liquidus interface towards the center of the casting at channels locations. As it moves to the center it gets hotter. Since the liquid was in equilibrium with solid at a lower temperature, it can induce remelting. Local Sn enrichment by the penetrating interdendritic liquid results in local depression of the liquidus temperature. Localized melting of solid dendrites occurs, the permeability increases with increasing liquid fraction, and hence the flow resistance decreases. The flow follows preferred channels which are indicated by the closely spaced streamlines shown in Figures 9 and 10.

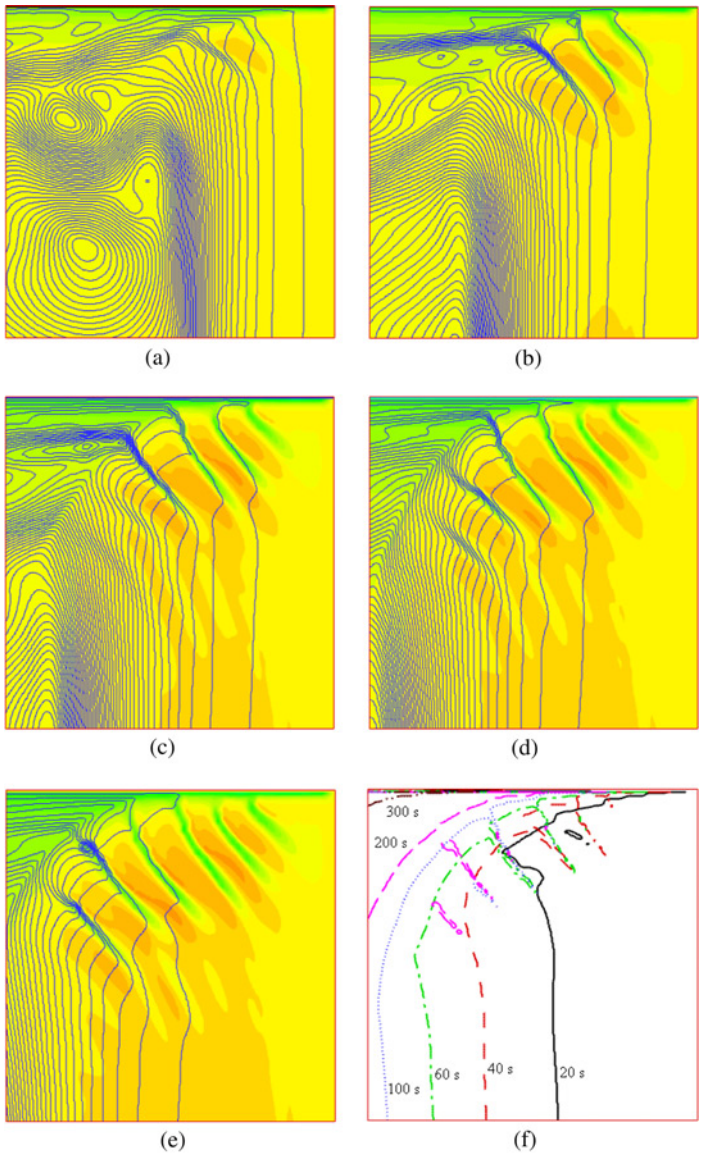

Notes: (a) Time 20 s; (b) time 40 s; (c) time 60 s; (d) time 100 s; (e) time 200 s; (f) front of mushy zone ($f_l = 0.95$) at different times

Figure 9.
Stages of development of channels segregates using TVD scheme (192 × 231 grid), zoom on the upper right corner of the cavity

The first developed channel is observed to form horizontally along the cavity top surface. Other channels start developing from the top to the bottom of the cavity. Once a channel is developed it starts elongating to connect with the top solute-rich region. The last developed channels may therefore not elongate to the top region as due to insufficient time to be completely established. This order of channels development is observed using either CD or TVD schemes. Closer look at the streamlines shows that for the development of a channel

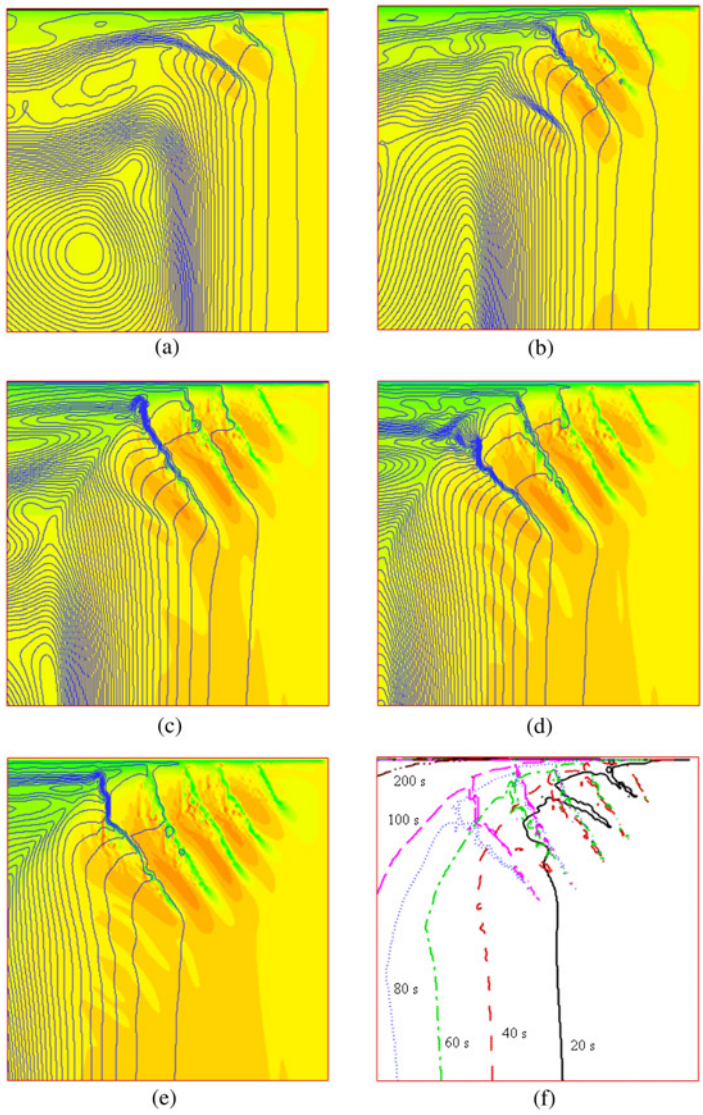

Notes: (a) Time 20 s; (b) time 40 s; (c) time 60 s; (d) time 100 s; (e) time 200 s; (f) front of mushy zone ($f_l = 0.95$) at different times

Figure 10.
Stages of development of channels segregates using CD scheme (192 × 231 grid), zoom on the upper right corner of the cavity

the streamlines are first disturbed in the new channel location and with the passage of time a channel is established at the new location. The reason for the disturbance of streamlines below an established channel is attributed to the tendency of flow to change orientation to feed the upper channel. This sequence can be observed for the development of all channels. Note also that the first channels formed at earlier times (20 s) change orientation with more tilted angle with the passage of time. This can be observed from the streamlines and concentration maps as well as from the liquid front map at different times.

Figure 11 shows the horizontal profiles of mixture composition at the end of solidification using different schemes (H1 at y = 10 mm, H2 at y = 30 mm, H3 at y = 50 mm). As compared to the results obtained using TVD schemes, irregularities of concentration values in the region of channels are predicted using the CD scheme. These are manifested by irregularities in flow streamlines passing through the channels.

7. Conclusions

Complex flow structures and sharp gradients in the solutal field associated with the development of flow channels call for the implementation of special non-oscillarity type high-order schemes to handle the regions of channels segregates. In the present study, a time-splitting approach has been adopted to separately handle solute advection and diffusion. This splitting technique allows the application of accurate total variation dimensioning schemes (TVD and WENO) for solution of solute advection. Solidification of a binary Pb-18%Sn alloy in a two-dimensional rectangular domain is considered for the analysis of thermo-solutal convection, channels formation, and macrosegregation fields obtained using different schemes. The governing equations for mass, momentum, energy, and species are based on the volume-averaging method.

Grid convergence patterns and numerical uncertainty are found to be dependent on the applied scheme. In general, the first-order hybrid scheme is highly diffusive and under predicts the formation of channels. Numerical diffusion associated with first-order schemes is non-negligible in the region of channels formation where the flow is oblique to the grid boundaries. The second-order central-difference scheme brings about oscillations

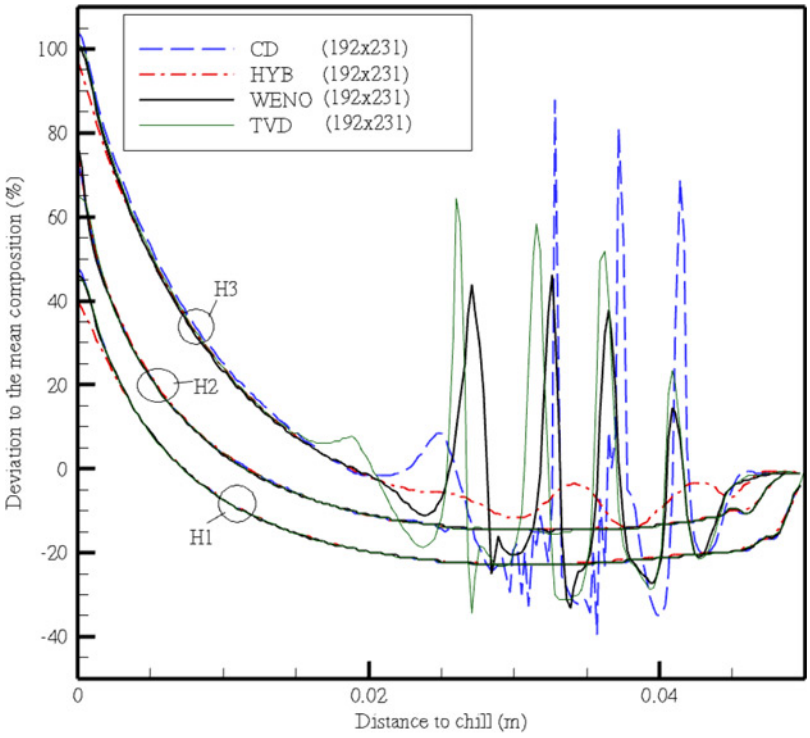

Notes: H1: y = 10 mm; H2: y = 30 mm; H3: y = 50 mm;

Figure 11.
Horizontal profiles of mixture composition at the end of solidification using different schemes

with possible non-physical extremes of solute composition in the region of channel segregates due to discontinuities in the solutal field. The results obtained using TVD and WENO schemes contain no oscillations and show an excellent capture of channels formation and resolution of the interface between solute-rich and depleted bands. Numerical results show the difficulty of obtaining grid-independent solutions with respect to local details in the regions of channels formations because of the highly unstable and transient convection phenomena. However, satisfactory grid-independent prediction of global extent of macrosegregation can be achieved.

A minimum number of nodes is required for resolving the flow characteristics and following the stages of development of channels. Since channel size (about 1,000 μm) is related to the value of dendrite arm spacing ($d_2 = 185$ μm in the present study), the minimum required grid size should be in the order of dendrite arm spacing in order to accurately predict channels formations. In areas away from the channels region the grid size is not critical and a coarser mesh can be used. However, considerable differences between the various simulations that are apparent on the local scale of a single channel indicate that the minimum spacing recommendation is not sufficient to achieve grid-independent results. The local scale phenomena in the channels region are better described by the increasing the number of nodes in the channel.

Different stages of channels formation are followed by analyzing thermo-solutal convection and macrosegregation at different times during solidification. The first developed channel is observed to form horizontally along the cavity top surface. Perturbations in the flow field in the region below the first channel, which are in the general form of oblique flow at the region of a channel formation, result in the development of other channels in a sequence that starts from the top towards the bottom of the cavity. The flow is perturbed because of the tendency to approach and feed a previously established upper preferred flow path. This perturbation induces remelting with a new established flow channel as the flow in the earlier one is decreased by the progress of solidification. Once a channel is developed it starts elongating to connect with the top solute-rich region. The last developed channels may therefore not elongate to the top region as due to insufficient time to be completely established. This order of channels development is observed using either CD or TVD schemes.

References

Amberg, G. (1991), "Computation of macrosegregation in an iron–carbon cast", *International Journal of Heat and Mass Transfer*, Vol. 34, pp. 217-27.

Beckermann, C. (2002), "Modelling of macrosegregation: applications and future needs", *International Materials Reviews*, Vol. 47, pp. 243-61.

Beckermann, C. and Viskanta, R. (1993), "Mathematical modeling of transport phenomena during alloy solidification", *Applied Mechanics Reviews*, Vol. 46, pp. 1-27.

Bennon, W.D. and Incropera, F.P. (1987), "A continuum model for momentum heat and species transport in binary solid–liquid phase change systems – I. Model formulation", *International Journal of Heat and Mass Transfer*, Vol. 30, pp. 2161-70.

Celik, I.B. and Li, J. (2005), "Assessment of numerical uncertainty for the calculations of turbulent flow over a backward-facing step", *International Journal for Numerical Methods in Fluids*, Vol. 49, pp. 1015-31.

Cless, C.M. and Prescott, P. (1996), "Effect of time marching schemes on predictions of oscillatory natural convection in fluids of low Prandtl number", *Numerical Heat Transfer Part A*, Vol. 29, pp. 575-97.

Felicelli, S.D., Heinrich, J.C. and Poirier, D.R. (1991), "Simulation of freckles during vertical solidification of binary alloys", *Metallurgical Transactions B*, Vol. 22, pp. 847-59.

Felicelli, S.D., Poirier, D.R. and Heinrich, J.C. (1997), "Macrosegregation patterns in multi-component Ni-base alloys", *Journal of Crystal Growth*, Vol. 177, pp. 145-61.

Fortin, M. and Glowinsky, R. (1982), "Méthodes de Lagrangien augmenté", Application *à la résolution numérique de problèmes aux limites'*, Dunod.

Ganesan, S. and Poirier, D.R. (1990), "Conservation of mass and momentum for the flow of interdendritic liquid during solidification", *Metallurgical Transactions B*, Vol. 21, pp. 173-81.

Gibou, F., Fedkiw, R., Caflisch, R. and Osher, S. (2003), "A level set approach for the numerical simulation of dendritic growth", *Journal of Scientific Computing*, Vol. 19, pp. 183-99.

Goyeau, B., Bousquet-Melou, P., Gobin, D., Quintard, M. and Fichot, F. (2004), "Macroscopic modeling of columnar dendritic solidification", *Computational and Applied Mathematics*, Vol. 23 Nos. 2/3, pp. 381-400.

Harten, A. (1983), "High resolution schemes for hyperbolic conservation laws", *Journal of Computational Physics*, Vol. 49, pp. 357-93.

Harten, A., Engquist, B., Osher, S. and Chakravarthy, S. (1987), "Uniformly high order essentially non-oscillatory schemes", *Journal of Computational Physics*, Vol. 71, pp. 231-303.

Hirsch, C. (1990), *Numerical Computation of Internal and External Flows*, Wiley, New York, NY.

Jiang, G.-S. and Shu, C.-W. (1996), "Efficient implementation of weighted ENO schemes", *Journal of Computational Physics*, Vol. 126, pp. 202-28.

LeVeque, R.J. (1990), Numerical methods for conservation laws, in Lanford, O.E. (Ed.), *Lecture in Mathematics*, Birkhauser, Zurich, p. 206.

Mohamad, A.A. and Viskanta, R. (1989), "An evaluation of different discretization schemes for natural convection of low-Prandtl-number fluids in cavities", *Numerical Heat Transfer Part B*, Vol. 16, pp. 170-92.

Ni, J. and Beckermann, C. (1991), "A volume-averaged two-phase model for solidification transport phenomena", *Metallurgical Transactions B*, Vol. 22B, pp. 349-61.

Oberkampf, W.L. and Trucano, T.G. (2008), "Verification and validation benchmarks", *Nuclear Engineering and Design*, Vol. 238, pp. 716-43.

Prescott, P.J. and Incropera, F.P. (1994), "Convective transport phenomena and macrosegregation during solidification of a binary metal alloy: I – numerical predictions", *Journal of Heat Transfer*, Vol. 116, pp. 735-41.

Prescott, P.J. and Incropera, F.P. (1996), "Convection heat and mass transfer in alloy solidification", *Advances in Heat Transfer*, Vol. 28, pp. 231-338.

Prescott, P.J., Incropera, F.P. and Bennon, W.D. (1991), "Modeling of dendritic solidification systems: reassessment of the continuum momentum equation", *International Journal of Heat and Mass Transfer*, Vol. 34, pp. 2351-9.

Rappaz, M., Bellet, M. and Deville, M. (2003), *Numerical Modeling in Materials Science and Engineering*, *Springer Series in Computational Mathematics*, Chapter 5, Springer-Verlag, Berlin, Heidelberg, New York, NY.

Roache, P.J. (1998), *Verification and Validation in Computational Science and Engineering*, Hermosa Publishers, Albuquerque, NM.

Schneider, M.C. and Beckermann, C. (1995), "Formation of macrosegregation by multicomponent thermosolutal convection during solidification of steel", *Metallurgical Transactions A*, Vol. 26, pp. 2373-88.

Shu, C.-W. (2003), "High-order finite difference and finite volume WENO schemes and discontinuous Galerkin methods for CFD", *International Journal of Computational Fluid Dynamics*, Vol. 17, pp. 107-18.

Shu, C.-W. and Osher, S. (1988), "Efficient implementation of essentially non-oscillatory shock capturing schemes", *Journal of Computational Physics*, Vol. 77, pp. 439-71.

Shu, C.-W. and Osher, S. (1989), "Efficient implementation of essentially non-oscillatory shock capturing schemes", *Journal of Computational Physics*, Vol. 83, pp. 32-78.

Sweby, P.K. (1984), "High resolution schemes using flux limiters for hyperbolic conservation laws", *SIAM Journal on Numerical Analysis*, Vol. 21, pp. 995-1011.

Sweby, P.K. (1985), "High resolution TVD schemes using flux limiters", *Lectures in Applied Mathematics*, Vol. 22, pp. 289-309.

Venneker, B.C.H. and Katgerman, L. (2002), "Modelling issues in macrosegregation predictions in direct chill castings", *Journal of Light Metals*, Vol. 2, pp. 149-59.

Vincent, S. and Caltagirone, J.P. (1999), "Efficient solving method for unsteady incompressible interfacial flow problems", *International Journal for Numerical Methods in Fluids*, Vol. 30, pp. 795-811.

Voller, V.R., Brent, A. and Prakash, C. (1989), "The modeling of heat, mass and solute transport in solidification systems", *International Journal of Heat and Mass Transfer*, Vol. 32, pp. 1719-31.

Wang, Y. and Hutter, K. (2001), "Comparisons of numerical methods with respect to convectively dominated problems", *International Journal for Numerical Methods in Fluids*, Vol. 37, pp. 721-45.

Yee, H.C. (1987), "Upwind and symmetric shock capturing schemes", NASA Technical Report, NASA-TM-89464.

Zhou, H. and Zebib, A. (1992), "Oscillatory convection in solidifying pure metals", *Numerical Heat Transfer Part A*, Vol. 22, pp. 435-68.

Further reading

Guo, J. and Beckermann, C. (2003), "Three dimensional simulation of freckle formation during binary alloy solidification: effect of mesh spacing", *Numerical Heat Transfer, Part A*, Vol. 44, pp. 559-76.

Prescott, P.J., Incropera, F.P. and Gaskell, D.R. (1994), "Convective transport phenomena and macrosegregation during solidification of a binary metal alloy: II – experiments and comparisons with numerical predictions", *Journal of Heat Transfer*, Vol. 116, pp. 742-9.

Sandham, N.D. and Yee, H.C. (1989), "A numerical study of a class of TVD schemes for compressible mixing layers", NASA.

Appendix

A.1 Lax-Wendroff TVD SUPERBEE scheme

The 1D Lax-Wendroff discretization of Equation (13) by a characteristic method in a finite-volume approximation is written as:

$$C_i^{n+1} = C_i^n - u\sigma(C_i^n - C_{i-1}^n) + \frac{1}{2}u\sigma\Delta x(u\sigma - 1)(\gamma_i^{nLW} - \gamma_{i-1}^{nLW}) \tag{A.1}$$

where $\sigma = \Delta t/\Delta x$ is the CFL number, $\gamma_i^{n,LW} = (C_{i+1}^n - C_i^n)/\Delta x$ corresponds to the Lax-Wendroff slope. To render the Lax-Wendroff TVD, the idea is to limit the slope $\gamma_i^{n,LW}$ to enforce the TVD requirements. The new limited slope is expressed as (Hirsch, 1990; Sweby, 1984, 1985):

$$\gamma_i^{n,T} = \max(0, \min(1, 2\theta_i^n), \min(2, \{\theta_i^n\}))\frac{C_{i+1}^n - C_i^n}{\Delta x} = \phi(\theta_i^n)\gamma_i^{n,LW} \tag{A.2}$$

where $\theta_i^n = (C_i^n - C_{i-1}^n)/(C_{i+1}^n - C_i^n)$. In fact, $\phi(\theta_i^n)$ is a correcting flux equal to 1 in the

whole solving domain, except near the extrema where this flux limits the Lax-Wendroff slope. This TVD scheme is called the Lax-Wendroff TVD SUPERBEE scheme. The final expression of C^{n+1} in 1D for any u is:

$$\begin{aligned} C_i^{n+1} = C_i^n - \sigma \max(0,u)(C_i^n - C_{i-1}^n) + \frac{1}{2}\sigma\Delta x \max(0,u)(u\sigma - 1) \\ \times (\phi_i^n \gamma_i^{nLW} - \phi_{i-1}^n \gamma_{i-1}^{nLW}) - \sigma \min(0,u)(C_{i+1}^n - C_i^n) \\ + \frac{1}{2}\sigma\Delta x \min(0,u)(u\sigma + 1)(\phi_{i+1}^n \gamma_{i+1}^{nLW} - \phi_i^n \gamma_i^{nLW}) \end{aligned} \tag{A.3}$$

The 2D and 3D form of Equation (A.3) is immediately deduced from a transposition of the x-direction flux to y- and z- directions. Solving the three directions at the same time may induce some distortions in the diagonal directions. As a consequence for 2D and 3D calculations, the time step is cut into two and three parts, respectively, and solution is obtained for one direction in each part. Considering V_x, V_y, and V_z as the velocities in each direction, the solution is obtained in three steps as: $C_{i,j,k}^{n+1/3} = f(C_{i,j,k}^n, V_x)$, $C_{i,j,k}^{n+2/3} = f(C_{i,j,k}^{n+1/3}, V_y)$, and $C_{i,j,k}^{n+1} = f(C_{i,j,k}^{n+2/3}, V_z)$ where the function f is given by the expression of Equation (A.1) using the corresponding velocity and concentration.

A.2 Fifth-order WENO scheme

To provide a description of the fifth-order finite difference WENO scheme (Jiang and Shu, 1996) in the simplest case, the 2D species conservation equation can be written as:

$$C_t + f(C)_x + g(C)_y = 0 \tag{A.4}$$

Before discussing the spatial discretizations of the derivatives $f(C)_x$ and $g(C)_y$, it should be mentioned that the time discretization of WENO scheme is implemented by a class of third order Runge-Kutta method for solving:

$$C_t = L(C,t) \tag{A.5}$$

Where L(C, t) is a discretization of the spatial operator. The third-order Runge-Kutta is simply described as:

$$\begin{aligned} C^{(1)} &= C^n + \Delta t\, L(C^n) \\ C^{(2)} &= \frac{3}{4}C^n + \frac{1}{4}C^{(1)} + \frac{1}{4}\Delta t\, L(C^{(1)}) \\ C^{n+1} &= \frac{1}{3}C^n + \frac{2}{3}C^{(2)} + \frac{2}{3}\Delta t\, L(C^{(2)}) \end{aligned} \tag{A.6}$$

A conservative finite difference spatial discretization to the conservation law given by Equation (A.4) approximates the derivative $f(C)_x$ by a conservative difference:

$$f(C)_x\big|_{x=x_j} = \frac{1}{\Delta x}\left(\hat{f}_{j+1/2} - \hat{f}_{j-1/2}\right) \tag{A.7}$$

where $\hat{f}_{j+1/2}$ is the numerical flux, which typically is a Lipschitz continuous function of several neighboring values C_j. $g(C)_y$ is approximated in the same way. For the simplest case of a scalar Equation (A.4) and if $f'(C) \geq 0$, the fifth-order finite difference WENO scheme has the flux given by (Shu, 2003):

$$\hat{f}_{j+1/2} = w_1\hat{f}_{j+1/2}^{(1)} + w_2\hat{f}_{j+1/2}^{(2)} + w_3\hat{f}_{j+1/2}^{(3)} \tag{A.8}$$

where $\hat{f}_{j+1/2}^{(i)}$ are three third-order fluxes on three different stencils given by:

$$\begin{aligned}\hat{f}_{j+1/2}^{(1)} &= \frac{1}{3}f(C_{j-2}) - \frac{7}{6}f(C_{j-1}) + \frac{11}{6}f(C_j)\\ \hat{f}_{j+1/2}^{(2)} &= -\frac{1}{6}f(C_{j-1}) + \frac{5}{6}f(C_j) + \frac{1}{3}f(C_{j+1})\\ \hat{f}_{j+1/2}^{(3)} &= \frac{1}{3}f(C_j) + \frac{5}{6}f(C_{j+1}) - \frac{1}{6}f(C_{j+2})\end{aligned} \tag{A.9}$$

and the non-linear weights w_i are given by:

$$w_i = \frac{\tilde{w}_i}{\sum_{k=1}^{3}\tilde{w}_k}, \quad \tilde{w}_k = \frac{\gamma_k}{(\varepsilon + \beta_k)^2} \tag{A.10}$$

with the linear weights γ_k given by:

$$\gamma_1 = \frac{1}{10}, \gamma_2 = \frac{3}{5}, \quad \gamma_3 = \frac{3}{10} \tag{A.11}$$

Finally, ε is a parameter to avoid the denominator to become zero and is usually taken as 10^{-6}. The smoothness indicators β_k are given by:

$$\begin{aligned}\beta_1 &= \frac{13}{12}\left(f(C_{j-2}) - 2f(C_{j-1}) + f(C_j)\right)^2 + \frac{1}{4}\left(f(C_{j-2}) - 4f(C_{j-1}) + 3f(C_j)\right)^2\\ \beta_2 &= \frac{13}{12}\left(f(C_{j-1}) - 2f(C_j) + f(C_{j+1})\right)^2 + \frac{1}{4}\left(f(C_{j-1}) - f(C_{j+1})\right)^2\\ \beta_3 &= \frac{13}{12}\left(f(C_j) - 2f(C_{j+1}) + f(C_{j+2})\right)^2 + \frac{1}{4}\left(3f(C_j) - 4f(C_{j+1}) + f(C_{j+2})\right)^2\end{aligned} \tag{A.12}$$

The scheme is proven to be uniformly fifth-order accurate including at smoothness extrema, and this is verified numerically. Detailed discussion of WENO scheme and generalization for complex situations are reported by Shu (2003) and Jiang and Shu (1996).

Corresponding author
Mohamed Rady can be contacted at: makrady@yahoo.com